applied sciences

MDPI

Article

Numerical and Field Investigations of Tremors Induced by Thick-Hard Strata Fracture

Ying Guo [1,2], Caiping Lu [1], Zhilong He [1,*] and Jiefang Song [1]

[1] Key Laboratory of Deep Coal Resource Mining (Ministry of Education), School of Mines, China University of Mining and Technology, Xuzhou 221116, China
[2] Baodian Coal Mine, Yankuang Energy Group Co., Ltd., Zoucheng 273513, China
* Correspondence: 18832059875@163.com

Abstract: Large energy mining-induced tremors are generally caused by the rupture of thick-hard overlying strata, and the roadway is prone to rockburst danger under its dynamic load. Through numerical simulations, the laws and influencing factors of stress, deformation, fracture and energy caused by mining-induced tremors (red bed breaking) were revealed, and the results were verified by field observations. The main conclusions were obtained: (1) the tensile stress and the compressive stress were concentrated in the middle of the thick-hard rock and both sides of the goaf, which were prone to tensile and shear failure type caused by mining-induced tremors, respectively; (2) after the goaf was formed, the compressive stress around the roadway was transformed into tensile stress. When a strong mining-induced tremor occurred, the tensile stress increased further. Meanwhile, when it was close to the tensile strength of the coal around the roadway, a rockburst occurred; (3) the energy of the mining-induced tremor released by shear failure was larger than that of the tensile failure. With the increase in shear strength of the roof, the released energy also increased; (4) according to the frequency-spectrum of the mining-induced tremors located in the extremely thick-hard overlying strata above the working face in the Baodian coal mine, the dynamic load generated by the tremors was superimposed on the high static load around the roadway, which was very likely to induce the instability of the roadway. The research conclusions have certain guiding significance for rockburst prevention in coal mines with thick-hard strata roofs.

Keywords: thick-hard overlying strata; rockburst; mining-induced tremors; microseismic monitoring; dynamic load

check for updates

Citation: Guo, Y.; Lu, C.; He, Z.; Song, J. Numerical and Field Investigations of Tremors Induced by Thick-Hard Strata Fracture. *Appl. Sci.* **2022**, *12*, 11151. https://doi.org/10.3390/app122111151

Academic Editor: Arcady Dyskin

Received: 9 September 2022
Accepted: 27 October 2022
Published: 3 November 2022

Publisher's Note: MDPI stays neutral with regard to jurisdictional claims in published maps and institutional affiliations.

Copyright: © 2022 by the authors. Licensee MDPI, Basel, Switzerland. This article is an open access article distributed under the terms and conditions of the Creative Commons Attribution (CC BY) license (https://creativecommons.org/licenses/by/4.0/).

1. Introduction

Mining-induced tremors are the most common dynamic phenomena in coal mines. When the accumulated stress reaches the peak strength of the coal and rock mass, the failure will occur, which will possibly induce the mining-induced tremors [1–3]. The occurrence of mining-induced tremors can be generally classified into three types: fault activation, roof breaking and coal pillar compression failure [4,5]. The tremors induced by the rupture of thick-hard strata are common in the Yanzhou coal mine district in China. For example, there is a rock stratum (commonly known as 'red bed') with a thickness of 50–300 m (more than 500 m in some areas) above the 3# coal seam in the Baodian, Nantun, and Dongtan coal mines. It is mainly composed of fine sandstone, which easily gathers plenty of elastic energy and causes the frequent occurrence of mining-induced tremors, due to fracture during the mining activity of working faces. The mining-induced tremors have a significant impact on safe production. Similar to natural earthquakes, high-scale events can cause tremors in surface buildings, coal and gas outbursts, and damage to support equipment. Especially, when the mining area is subjected to high static stress, the dynamic load released by the tremors will further make the coal and rock mass develop to the ultimate instability state until a rockburst is induced [6–8].

Scholars have conducted many studies on the occurrence mechanism of mining-induced tremors. For example, Kamila et al. used satellite interferometry to study the surface subsidence caused by mining-induced tremors [9]. Łukasz et al. suggested a method to fit the mining volume of the coal body and the energy released by mining-induced tremors [10]. Zhang et al. monitored the MS events in the mining process through using a self-built, high-precision MS monitoring system, and analyzed the change characteristics of the MS parameters before the occurrence of two rockburst accidents [11]. Ma et al. studied the ground tremors induced by different failure forms, and found that the ground tremor was mainly determined by the focal mechanism, distance, and azimuth [12]. Beata et al. studied the static stress transfer in the surrounding rock caused by two high energy events, based on the focal mechanism [13]. Ma et al. studied the relationship between the b value and MS events, and found that the b value tended to decrease before the high energy event, and increase significantly during the event [14]. Zhao et al. proposed a calculation method of rock damage, stress, and strain, defined by a focal moment tensor (MT), and studied its trend in work face mining [15].

In addition to field investigation, many researchers have also conducted fruitful studies in the numerical simulation of mining-induced tremors. For example, Islam et al. used the boundary element method to simulate the instability of a fault caused by the mining, indicating that the mining led to the increase of deviatoric stress around the fault and promoted the fault instability [16]. A simplified numerical model was developed to calculate the potential seismic response of the faults to the undercut advance [17]. Li et al. extended the implicit to explicit sequential solution method (IESSM) in Ansys/Ls-dyna to explore the failure behavior of an underground chamber caused by static in-situ stress and mining-induced tremor disturbance [18]. Meng et al. studied the influence of the dynamic load generated by different angles of roof fracture on gob side entry retention [19]. Zhu et al. discussed the influence of mining-induced tremor disturbance on the stability of an underground opening as its increasing magnitude and prolonged duration through rock failure process analysis (RFPA) software [20]. The above research undoubtedly enable us to have a deeper understanding of the mechanism of mining-induced tremors. However, due to the complexity of the mechanism of tremors, there are still many aspects to be further considered. In previous numerical simulations, the source of the tremor event was simplified as a trigonometric function or waveform, which is quite different from the actual source wavefield characteristics.

Moreover, the stress evolution process and fracture characteristics of tremor sources are often neglected in the field of numerical simulation. To make up for the defects in these works, this paper uses Universal Distinct Element Code (UDEC) software to reproduce the process of rockburst induced by mining-induced tremors generated by the fracture of thick-hard strata. The source was independently excited by weakening the rock parameters, which reproduced the stress concentration of the roadway caused by the fracture process of upper thick-hard strata and the mining-induced tremors. The influence of the fracture form and shear strength of the tremor source on the dynamic disturbance intensity of the roadway was discussed in detail. Finally, the numerical simulation conclusions were verified by field observations of mining-induced tremors caused by the thick-hard red bed fracture above the $73_{upper}07$ working face of the Baodian coal mine. The research conclusions have great reference significance for revealing the mechanism of mining-induced tremors induced by thick-hard strata fracture.

2. Numerical Simulation

2.1. Modelling

The UDEC can be used to simulate the deformation and failure process of discontinuous materials. In this software, the general numerical model is mainly composed of block elements and the interfaces among them. The block can be deformed but not destroyed. When the shear stress/tensile stress of interface exceeds its shear/tensile strength, the interface will be damaged, and the blocks bonded by that interface will be separated, which

means that cracks have occurred in the material. Therefore, UDEC can be used to simulate the fracture process of rock and the occurrence of rockburst.

Based on the actual geological conditions of the $73_{upper}07$ working face, a simplified numerical model was established to study the occurrence of rockburst around the roadway due to the disturbance of strong mining tremors by the fracture of thick-hard stratum. As shown in Figure 1, the height and width of the numerical model were 650 m and 437 m, respectively, and contained seven layers of rock. The goaf in the middle of the model with a height of 8 m and a width of 250 m was represented by a rectangular cave. The roadway with a width of 4 m was 200 m from the left boundary. In order to reduce the computing resource consumption while ensuring calculation accuracy, the different areas of the model were finely divided through different types of blocks. The thickness of the floor, 3# coal seam, immediate roof, primary roof #1, primary roof #2, red bed, and overburden were 19 m, 8 m, 10 m, 25 m, 35 m, 100 m, and 240 m, respectively.

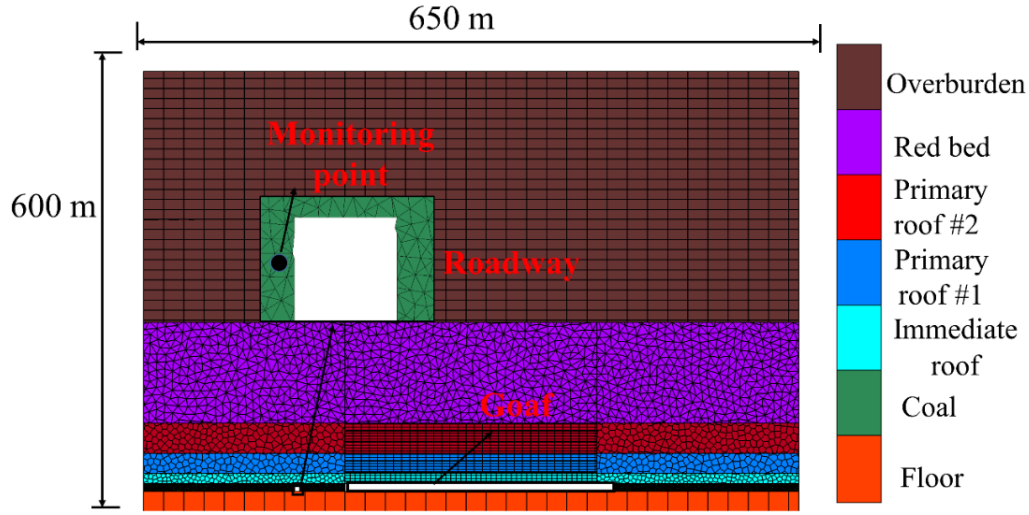


Figure 1. Numerical model.

There was a red bed with a thickness of 250 m above the 3# coal seam. The micro-parameters of the blocks and interfaces of different strata were calibrated based on the laboratory experiment, as shown in Tables 1 and 2. After the goaf was formed, the stress around the goaf would be transferred as the fall of the immediate roof and primary roof #1, causing the concentration of shear stress at the end of the red bed and the accumulation of a large amount of elastic energy. Under the influence of lateral abutment pressure, the stress around the roadway also rose sharply. When the concentrated stress reached the bearing strength of the red bed, it would fracture and generate mining-induced tremors. Besides, when the stress wave was interacted with the pre-existing high static load, the risk of the roadway rockburst would obviously increase.

Table 1. Micro-parameters of the block.

Stratum	Lithology	Density/(kg/m^3)	Bulk Modulus/GPa	Shear Modulus/GPa	Thickness/m
Floor	Siltstone #1	2600	5.47	2.82	19
Coal		1400	2.87	1.48	8
Immediate roof	Siltstone #2	2500	5.47	2.82	10
Primary roof #1	Medium sandstone	2600	6.42	2.56	25
Primary roof #2	Mudstone	2600	4.58	2.06	35
Thick-hard rock	Fine sandstone	2600	8.51	2.36	100
Overburden	Clay	2600	3.65	1.6	240

Table 2. Micro-parameters of the interface.

Lithology	Normal Stiffness/(GPa/m)	Tangential Stiffness/(GPa/m)	Cohesion/MPa	Friction Angle/°	Tensile Strength/MPa
Siltstone 1	30	12	1.2	36	1.54
Coal	28	11.2	1.6	20	1.2
Siltstone 2	25	12	1.6	10	1
Medium sandstone	40	21	1.6	10	1.2
Mudstone	36	18	1.6	10	1.2
Fine sandstone	76	30	8	60	5
Clay	20	8	1.3	25	1

2.2. Simulation

The simulation process was divided into two steps: static calculation and dynamic calculation. Before calculating, the vertical displacements between the two sides and the bottom of the model were fixed, but the top was free. A vertical stress of 15 MPa was applied on the top of the model, which represented the overburden of the coal seam with a burial depth of about 600 m. After static stress equilibrium, the roadway and goaf were excavated first, and then the stress redistribution caused by the roof fall above the goaf was observed. After that, the shear strength of the source was adjusted to 0, so that the red bed was fractured and the mining-induced tremors by dynamic distrubence could occur. The dynamic response of the roadway under the stress wave was measured.

2.3. Results and Analysis

2.3.1. Static Stress Evolution

Thick-Hard Roof Fracture

The stress redistribution characteristics in different areas of overlying strata before and after goaf formation are shown in Figure 2, in which the negative and positive values represent the compressive stress and the tensile stress, respectively. Obviously, due to the fall of the fractured strata above the goaf, the stress distribution at different positions of the red bed had obvious differences. High compressive stress concentration easily occurred at both ends of the red bed, and shear failure easily appeared. The central part of the red bed had a high tensile stress concentration area, which was prone to tensile failure. Due to the strata fracture, the internal stress of the overlying roof was redistributed, resulting in plenty of elastic strain energy accumulated in the surrounding rock. Once the roof fractured, it generated strong tremors. Figure 3 shows the stress redistribution characteristics around the roadway before and after the goaf formation.

As seen in Figure 3, the horizontal tensile stress of the two sides was concentrated after the roadway excavation. With the formation of the goaf and the increase in the lateral abutment pressure, the maximum horizontal tensile stress increased from 0.4 MPa to 10 MPa. Besides, the horizontal compressive stress in the roof was transferred to the deep, and the surface varied from compressive to tensile stress. Considering the tensile strength of the coal and rock was lower than its compressive strength, the roadway surface was the most prone to tensile failure under static load, resulting in a coal split. Meanwhile, the vertical stress distribution was similar to that of the horizontal stress. After the roadway excavation, the surface tensile stress was dominant, and the local compressive stress was concentrated at the corners. After that, the concentration degree and range of the tensile stress on the roadway surface gradually increased with the bend and subsidence of the red bed above the goaf, while the compressive stress gradually decreased, and thus the stability of the roadway reduced. It can be indicated that the stress around the roadway was redistributed after the excavation of the roadway, and it was gradually close to the critical instability state. After that, when the overlying thick-hard strata broke and produced strong tremors, the roadway was likely to fail and experience instability under the strong dynamic load disturbance superimposed by high static stress.

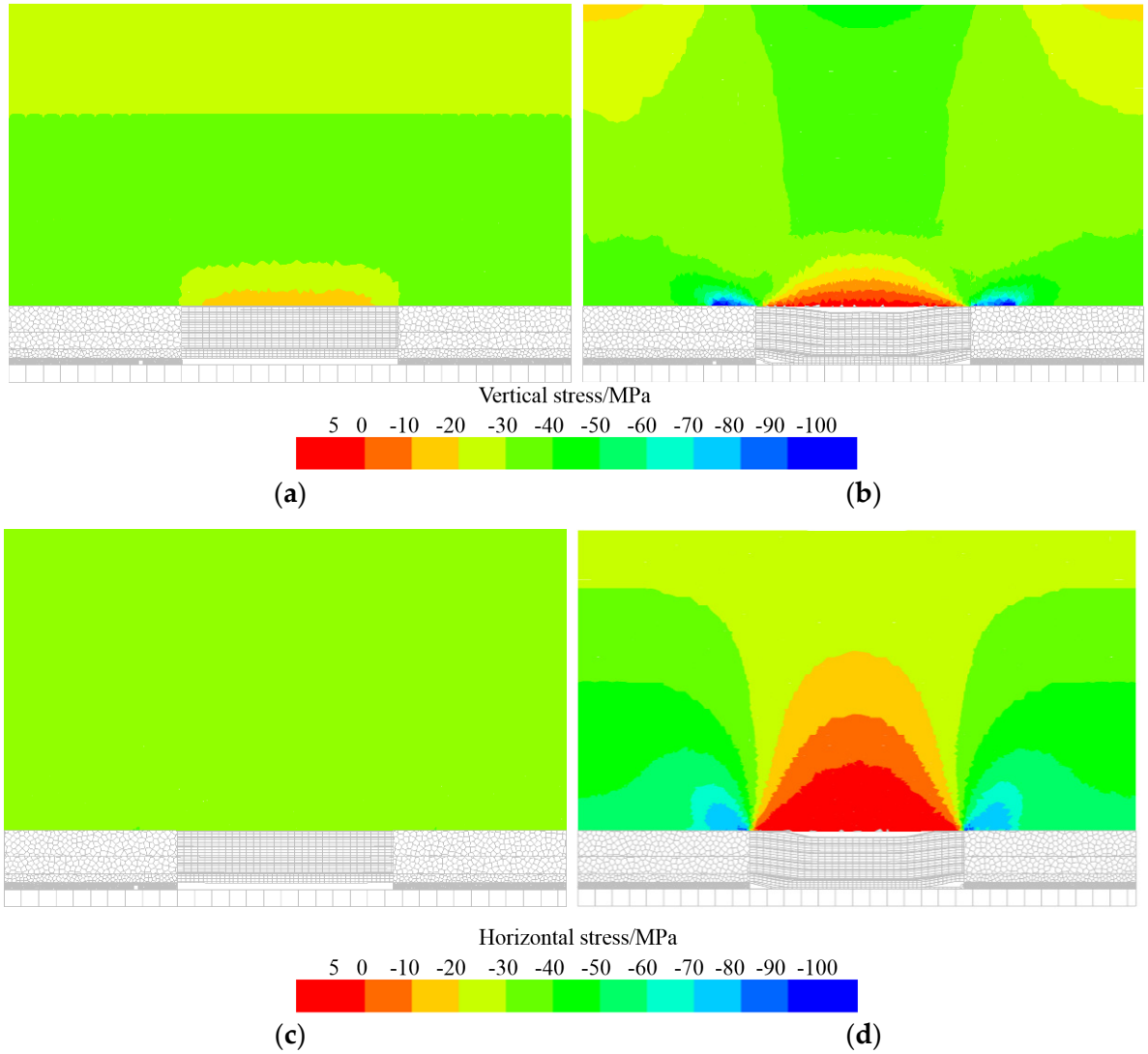


Figure 2. Stress distribution of overlying strata before and after goaf formation: (**a**) Vertical stress before goaf formation; (**b**) Vertical stress after goaf formation; (**c**) Horizontal stress before goaf formation; (**d**) Horizontal stress after goaf formation.

Influence of Tremors on Roadway

The velocity propagation cloud diagrams after the occurrence of a strong mining-induced tremor in the thick-hard rock layers are shown in Figure 4.

From Figure 4, the velocity diffused outward in an arc from the four corners of the rectangular source and gradually intersected into a circle with the increasing propagation distance, with a maximum velocity of 10 m/s. At 40 ms, the stress wave reached the roadway, resulting in the rapid increase in speed from 0 m/s to 2 m/s around the roadway. As shown in Figure 5, the kinetic energy rapidly reached the peak value of 7.5×10^6 J within 10 ms, and then begins to decrease gradually. At 106 ms, the stress wave excited by the source transmitted to the roadway, and the kinetic energy of the roadway began to increase and reach a peak of 3.1×10^4 J at 148 ms. Then, under the effect of damping, the kinetic energy of the roadway gradually decreased to 0. Obviously, the propagation disturbance of the tremor input a large amount of kinetic energy to the roadway. Under the strong disturbance of the tremor, the stress of the surrounding rock of the roadway was sharply adjusted, resulting in a gradual increase in the vibration speed. Finally, the surrounding rock was ruptured suddenly. The maximum vibration speed reaches approximately 10 m/s, and a rockburst was inevitably triggered.

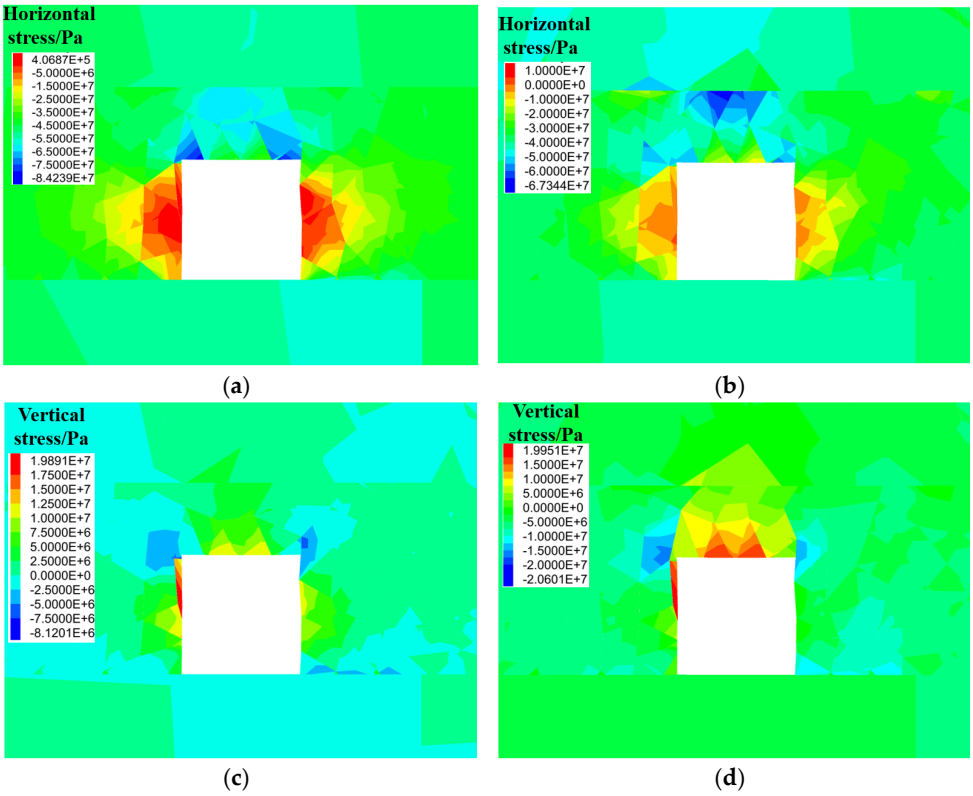


Figure 3. Stress redistribution surrounding the roadway before and after goaf formation: (**a**) Horizontal stress before goaf formation; (**b**) Horizontal stress after goaf formation; (**c**) Vertical stress before goaf formation; (**d**) Vertical stress after goaf formation.

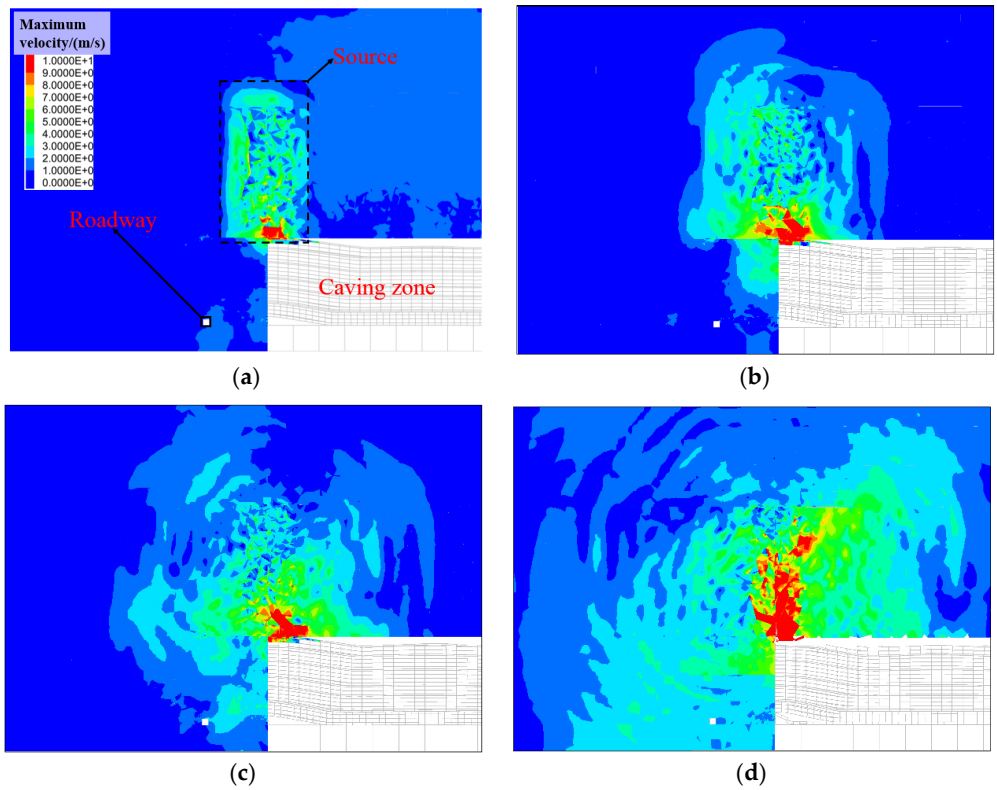


Figure 4. Velocity cloud diagram after mining-induced tremor: (**a**) 10 ms; (**b**) 20 ms; (**c**) 30 ms; (**d**) 40 ms.

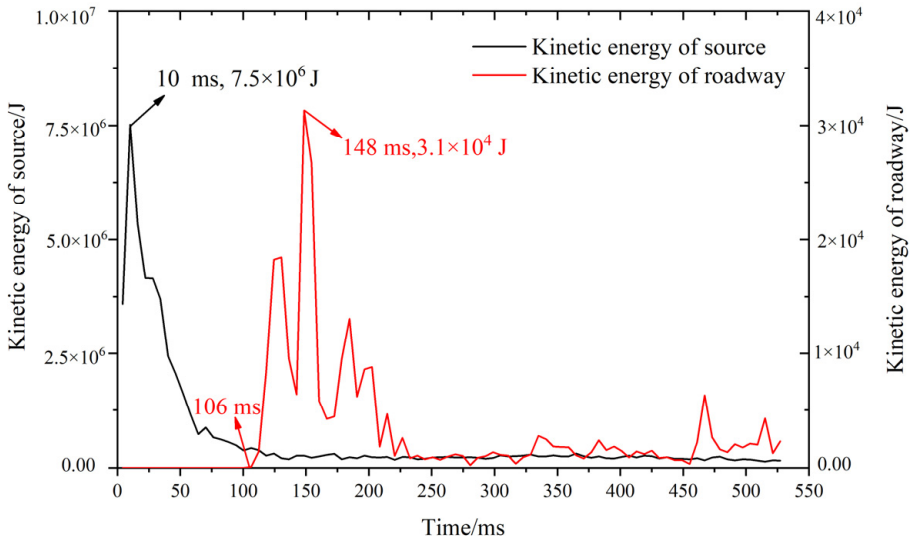


Figure 5. Kinetic energy curves of roadway and source after mining-induced tremor.

2.3.2. Evolution of Stress, Displacement and Fracture

The variations in maximum principal stress around the roadway due to the disturbance of a mining-induced tremor are shown in Figure 6.

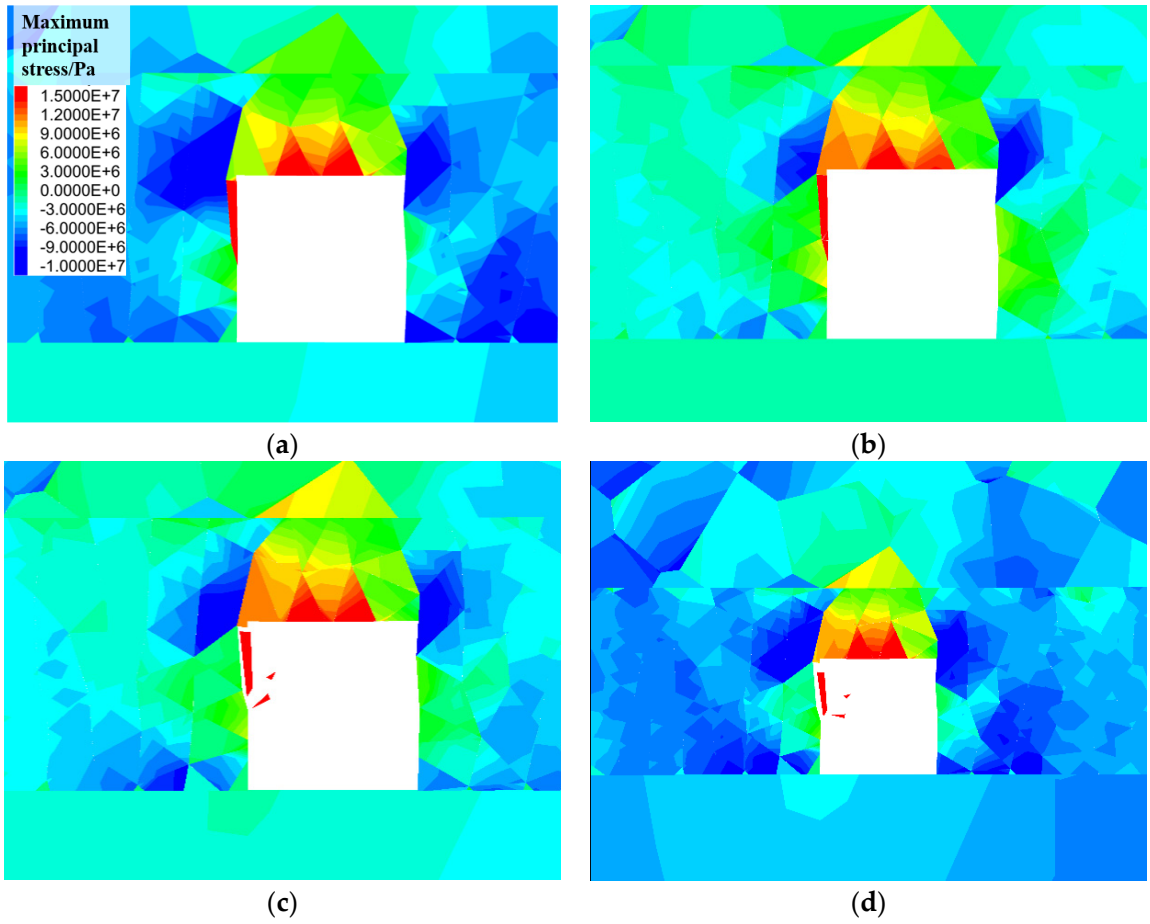


Figure 6. Evolution of maximum principal stress around the roadway: (**a**) 0 ms; (**b**) 100 ms; (**c**) 200 ms; (**d**) 300 ms.

As seen in Figure 6, the stress on the surface of both sides of the roadway transformed from the compressive to tensile state after the stress wave reached the roadway at 100 ms. At 200 ms, the tensile stress on the roadway surface gradually increased. When the tensile stress reached the tensile strength of the surrounding coal and rock, the coal mass on the left side ruptured. Subsequently, it fell and ejected into the roadway, and a rockburst inevitably occurred. At 300 ms, the stress of the surrounding coal and rock mass of the roadway redistributed, and the compressive stress continued to transfer to the roadway surface and return to the initial stress state. Figure 7 shows the variations in vertical stress, displacement, and crack number around the roadway during the whole process of tremor disturbance.

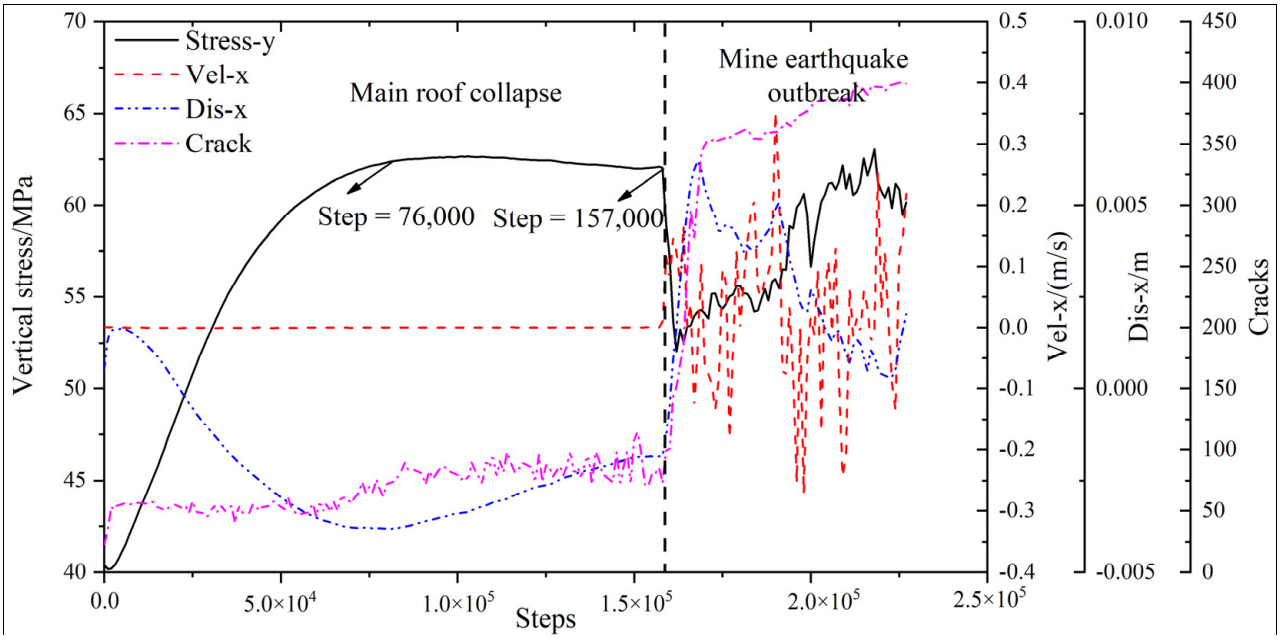


Figure 7. Variation curves of vertical stress, displacement and crack number around the roadway.

As seen in Figure 7, the stress, deformation velocity, displacement of the roadway, and the crack number around the roadway during the roof caving process (the monitoring points are shown in Figure 1) were recorded. Obviously, the initial vertical stress on the right side of the roadway was only 40 MPa, and began to rise gradually when the primary roof began to fracture and sink. Due to the high load, the surrounding coal and rock of the roadway were gradually damaged, the crack number began to increase, and the displacement of the roadway also increased accordingly. When the calculation step was 76,000, the movement of the primary roof had basically reached stability. At this time, the vertical stress did not increase and basically remained stable. As the calculation step reached 157,000, the stress wave arrived at the roadway. The vertical stress of the monitoring point dropped sharply, which may have been caused by the tensile stress generated by the stress wave. The vertical stress at this point was originally compressive stress, and decreased after tremor disturbance. Subsequently, the total number of cracks suddenly increased, and the corresponding vibration velocity fluctuated violently, indicating that the monitoring point was subjected to the repeated tensile and compressive actions of the focal stress wave. Finally, the number of cracks around the roadway reached a peak, which indicated that the damage to the roadway was more serious.

2.3.3. Analysis of Main Influencing Factors

Rupture Form

According to the previous analysis, after the primary roof fall was completed, the central part of the red bed would be unloaded and the tensile stress would be concentrated, while the shear stress at the two ends supported above the goaf would be concentrated.

Therefore, the tensile and shear rupture may have occurred in the middle and at two ends of the red bed, respectively, which would generate tremors. In order to compare the rockburst risk in these two cases, the central tensile strength and the end shear strength of the red bed were respectively reduced to 0 in order to excite the tremors, so as to compare the kinetic energy changes of the source and the roadway.

As seen in Figure 8a, when the calculation step was 1000, the peak kinetic energy was 7.5×10^6 J. However, the energy in the middle tensile failure zone was 3.7×10^5 J at the 3000th calculation step, and the stress threshold of tensile fracture was lower than that of the shear fracture. At the same time, the tensile strength of the rock was far lower than the shear strength, the energy radiated by the source was smaller, and the shear deformation accumulated more elastic strain energy, resulting in stronger tremors. Accordingly, under the shear rupture condition, the kinetic energy of the roadway was 3.1×10^4 J at the 12,000th calculation step, while the peak energy was 6.5×10^3 J under the tensile fracture condition (89,000th calculation step). Compared with the shear fracture, it took longer for the roadway kinetic energy to reach the peak value in the tensile fracture zone, which was obviously caused by the relative position between the failure and the focal.

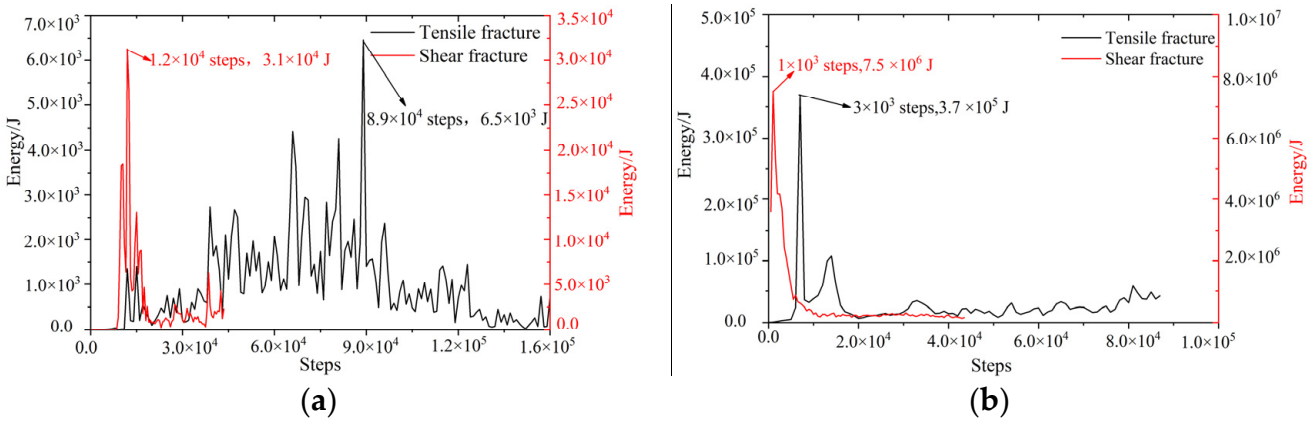


Figure 8. Kinetic energy change curves of source and roadway under different fault forms: (**a**) Source kinetic energy; (**b**) Roadway kinetic energy.

Rock Properties

From the above analysis, it can be seen that the occurrence of tremors was mainly caused by the shear fracture of thick-hard roof, and the strength of the red bed fracture inevitably affected the energy of the source. Therefore, three groups of simulations were conducted on the basis of the original model, and the ratios of shear strength were set to be 1.2, 0.8, and 0.6, respectively. Meanwhile, the kinetic energy radiated from the source during the whole process of roof rupture was monitored and analyzed. Figure 9 shows the kinetic energy curves of the roof fracture with different shear strengths.

As seen in Figure 9, the peak value of energy radiated by the source gradually decreased with the decreasing shear strength of the thick-hard roof. When the ratio of shear strength reduced from 1.2 to 1, the peak energy reduces from 8.3×10^6 J to 7.5×10^6 J, and the decrease was 0.8×10^6 J. When the ratio decreases from 1 to 0.8, the peak energy decreases by 5.9×10^6 J. The peak energy dropped by 1.55×10^6 J when the ratio decreased from 0.8 to 0.6. Therefore, the energy radiated by the source obviously increased with the increase in shear strength. However, the energy of the source would have hardly risen with the continuous increase in the shear strength of the rock, which may have been related to the energy storage limit of the rock.

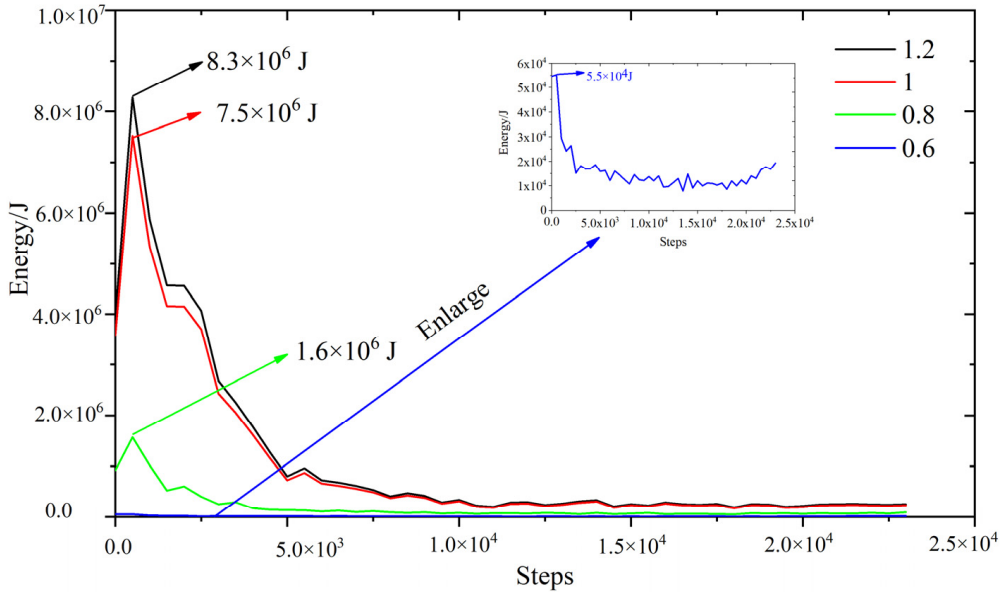


Figure 9. Kinetic energy curves of roof fracture with different shear strength.

3. Field Observations and Verification

The $73_{upper}07$ working face of the Baodian coal mine is located in the No. 7 mining area, with an average burial depth of 591.8 m. The working face is close to the boundary coal pillar between the Baodian and the Dongtan coal mines, and is adjacent to the goaf of the $73_{upper}05$ working face and the $73_{upper}09$ working face in the south and north directions, respectively. The mining seam of the working face is the 3_{upper} coal seam, with an buried depth of −536 m−−565 m and a thickness of 3.00–5.55 m (the average is 5.38 m). The immediate roof of the $73_{upper}07$ working face is mudstone, with an average thickness of 1.20 m, which has low strength and can easily fall. The primary roof #1 is sandstone with an average thickness of 18.60 m. The primary roof #2 is mudstone with an average thickness of 40.28 m, and upper statum is the red bed with a thickness of 250–300 m. In addition, the red bed has high strength, huge thickness, and does not easily deform or break. A MS monitoring system was installed in the Baodian coal mine, which could accurately locate and record MS events by receiving the elastic waves radiated by coal and rock ruptures. Figure 10 shows the plane and spatial distributions of mining-induced tremors in the coal and rock during the mining process of the $73_{upper}07$ working face.

According to the borehole column of rock strata in the $73_{upper}07$ working face, the immediate roof and the primary roof 2# were mudstone, and the primary roof 1# was relatively fractured. Therefore, the low-level roof strata could break and fall quickly after goaf formation. The red bed stratum was mainly composed of fine sandstone, with higher strength and thickness, which is not easy to fracture synchronously with the low-level rock. Based on the previous simulation results, the high tensile stress and compressive stress may be easily concentrated in the middle and at two ends of the red bed, respectively. When the concentrated stress reaches the strength limit of the rock, the rock would fracture, and a strong tremor would occur. As seen in Figure 10a, high-energy events were generally concentrated in the primary roof 2# and the red bed. In addition, the $73_{upper}07$ working face is adjacent to the 73_{upper} 05 goaf. Under the action of lateral abutment pressure, the headentry of the $73_{upper}07$ working face was in a state of high static stress. When the superimposed stress of static load and dynamic load by strong tremor exceeded the strength limit of the surrounding rock, the risk of rockburst increased sharply. As seen in Figure 10b, the high-energy events at the headentry near the 73_{upper} 05 goaf were significantly more than that at the tailentry, indicating that the area was in a state of high stress concentration. Previous studies have shown that the dominant frequency of seismic wave has a significant difference with different breaking scales of the source. The lower the dominant frequency

of the source was, the larger the rupture scale would be. To further study the fracture characteristics of the red bed, the event 1# with the maximum energy in the red bed was selected to conduct spectrum analysis, and the results are shown in Figure 11.

As seen in Figure 11a, the duration of this strong tremor was long, and the energy attenuation was slow. As seen in Figure 11b, the spectrum distribution characteristics of the event received by different geophones were similar and the dominant frequency was lower. The dominant frequencies of the waveforms received by #3, #4, #5, and #6 geophones were 2.9 Hz, 5.3 Hz, 3.0 Hz and 4.3 Hz, respectively. In addition, the energy was mainly concentrated in the frequency range of 0–10 Hz, indicating that large-scale rupture occurred in the red bed, due to local stress concentration. When the amplitude was constant, the frequency of the stress wave was lower, the attenuation of the energy in the propagation process was slower, and the energy transmitted to the roadway was higher. Meanwhile, the large-scale rupture of the red bed may have induced the overall activity of the fractured strata, and caused sudden increases in the roadway stress, which could induce large and violent deformation of the roadway, support damage, and other dynamic phenomena.

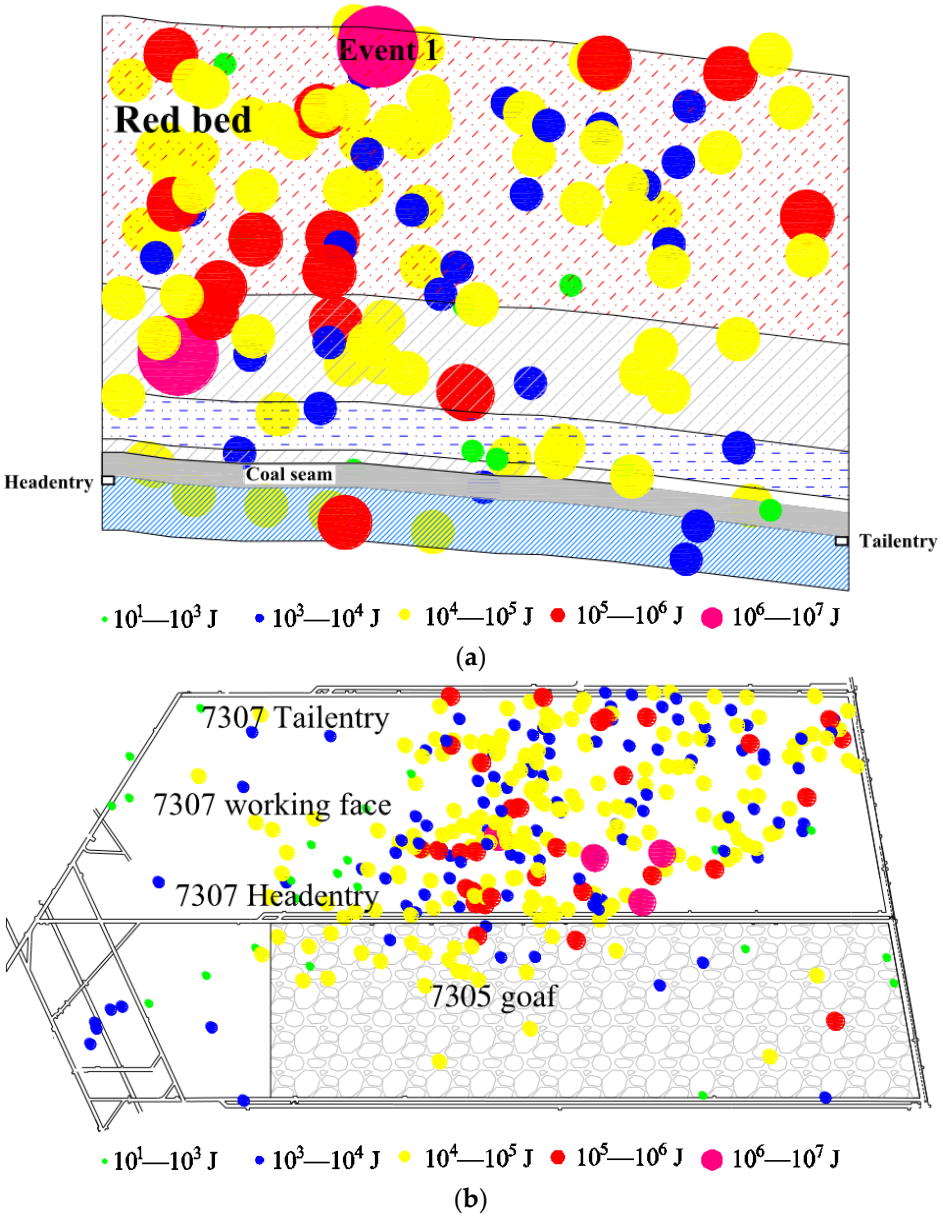
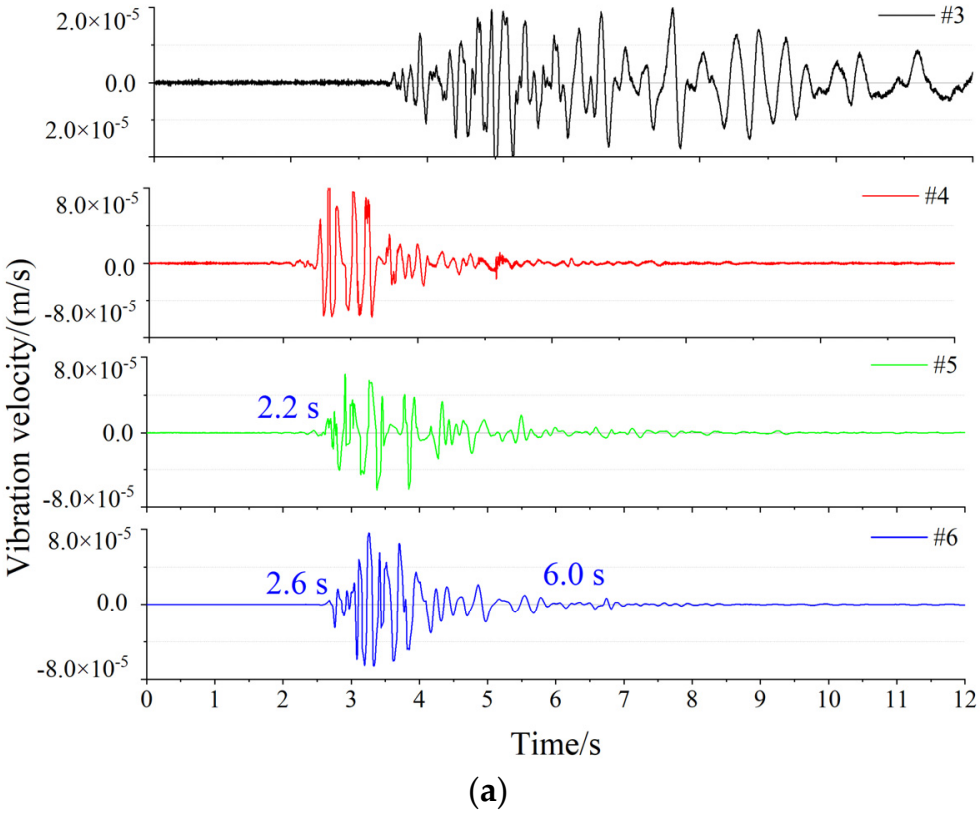


Figure 10. *Cont.*

Position	Stratum	Bore illustration	Average thickness(m)
Jurassic red bed	Fine sandstone		275.00 m
#2 Primary roof	Mudstone #2		40.28 m
#1 Primary roof	Siltstone #2		18.60 m
Immediate roof	Mudstone #1		1.20 m
Coal	Coal		5.38 m
Floor	Siltstone #1		16.54 m

(**c**)

Figure 10. Distributions of tremor sources during mining process of the working face: (**a**) Spatial distribution of sources; (**b**) Plane distribution of sources; (**c**) Column of coal and rock strata.



(**a**)

Figure 11. *Cont.*

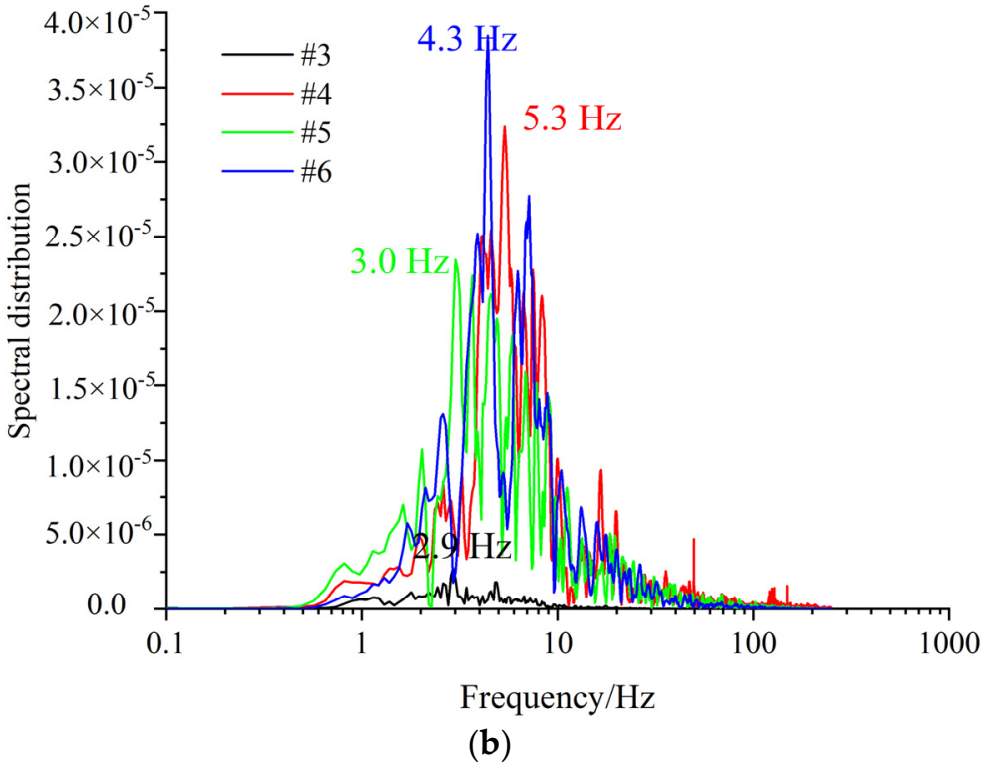


Figure 11. Waveforms and spectrum distributions of strong tremor event #1: (**a**) Waveforms received by different geophones; (**b**) Spectrum distributions.

4. Conclusions

(1) After the formation of the goaf, the tensile stress in the middle of the thick-hard stratum was concentrated, and the compressive stress on both sides of the goaf was concentrated. Therefore, the central and end parts easily produced tensile and shear failure, respectively.

(2) The whole process of roadway failure induced by the superposition of dynamic and static loads was simulated in detail. First, the state of the roadway surface changed from compressive to tensile stress once the goaf was formed. After the arrival of the stress wave generated by a tremor, the tensile stress on the roadway surface further increased until it exceeded the tensile strength, and the surrounding coal and rock gradually broke and led to a rockburst occurring.

(3) The influencing laws of the source rupture form of the thick-hard strata and corresponding shear strength on the tremors were analyzed in detail. It was found that the released energy of the shear failure was greater than that of the tensile failure. In addition, with the increase in the shear strength of the thick-hard rock, the released energy from the source also increased.

(4) Using field observations, the strong tremors in the $73_{uppper}07$ working face in the Baodian coal mine were analyzed. Spectrum analysis showed that the dominant frequency of the tremor was lower, the duration was longer, and the energy attenuation was slower, indicating a large-scale rupture of the red bed. When the high static load near the roadway was superimposed with dynamic disturbance by tremors, it was very likely to induce a rockburst.

Author Contributions: Software, Z.H.; Supervision, J.S.; Writing—original draft, Y.G.; Writing—review & editing, C.L. All authors have read and agreed to the published version of the manuscript.

Funding: This research was funded by the National Natural Science Foundation of China. The grant number is [51574225].

Institutional Review Board Statement: Not applicable.

Informed Consent Statement: Not applicable.

Data Availability Statement: Not applicable.

Acknowledgments: We gratefully wish to acknowledge the collaborative funding support from the National Natural Science Foundation of China (51574225). The data used in this study are available from the authors.

Conflicts of Interest: The authors declare no conflict of interest.

References

1. Zhang, X.; Feng, X.P.; Li, D.H.; Yin, F.L.; Yi, L. Diverse rupture processes of the 2014 Kangding, China, earthquake doublet (MW 6.0 and 5.7) and driving mechanisms of aftershocks. *Tectonophysics* **2021**, *820*, 229118. [CrossRef]
2. Hosseinzadehsabeti, E.; Ferr'e, E.C.; Persaud, P.; Fabbri, O.J.; Geissman, W. The rupture mechanisms of intraslab earthquakes: A multiscale review and re-evaluation. *Earth-Sci. Rev.* **2021**, *221*, 103782. [CrossRef]
3. Wasilewski, S. Gas-dynamic phenomena caused by rock mass tremors and rock bursts. *J. Min. Sci. Technol.* **2020**, *30*, 8. [CrossRef]
4. Lu, C.P.; Liu, Y.; Liu, G.J.; Zhao, T.B. Stress evolution caused by hard roof fracturing and associated multi-parameter precursors. *Tunn. Undergr. Space Technol.* **2019**, *84*, 295–305. [CrossRef]
5. Lu, C.P.; Liu, G.J.; Liu, Y.; Zhang, N.; Xue, J.H.; Zhang, L. Microseismic multi-parameter characteristics of rockburst hazard. *Int. J. Rock Mech. Min. Sci.* **2015**, *76*, 18–32. [CrossRef]
6. Szurgacz, D. Electrohydraulic control systems for powered roof supports in hazardous conditions of mining tremors. *J. Sustain. Min.* **2015**, *14*, 157–163. [CrossRef]
7. Kuzniar, K.; Zajac, M. Numerical evaluation of natural vibration frequencies of thermo-modernized apartment buildings subjected to mining tremors. *Procedia Eng.* **2017**, *199*, 296–301. [CrossRef]
8. Cielik, J.; Burtan, Z.; Chlebowski, D. Geomechanical analysis of location and conditions for mining-induced tremors in LGOM copper mines. *J. Sustain. Min.* **2017**, *16*, 94–103. [CrossRef]
9. Kamila, P.; Andrzej, B. Mining-induced tremors in the light of deformations estimated by satellite SAR interferometry in the Upper Silesian Coal Basin, Poland. *Procedia Comput. Sci.* **2021**, *181*, 685–692.
10. Wojtecki, L.; Kurzeja, J.; Knopik, M. The influence of mining factors on seismic activity during longwall mining of a coal seam. *Int. J. Rock Mech. Min. Sci.* **2021**, *31*, 429–437. [CrossRef]
11. Zhang, C.; Jin, G.H.; Liu, C.; Li, S.G.; Xue, J.H.; Cheng, R.H.; Wang, X.L.; Zeng, X.Z. Prediction of rockbursts in a typical island working face of a coal mine through microseismic monitoring technology. *Tunn. Undergr. Space Technol.* **2021**, *113*, 103972. [CrossRef]
12. Ma, J.; Dong, L.J.; Zhao, G.Y.; Li, X.B. Ground motions induced by mining seismic events with different focal mechanisms. *Int. J. Rock Mech. Min. Sci.* **2021**, *116*, 99–110. [CrossRef]
13. Orlecka-Sikora, B.; Lasocki, S.; Lizurek, G.; Rudzin´, L. Response of seismic activity in mines to the stress changes due to mining induced strong seismic events. *Int. J. Rock Mech. Min. Sci.* **2012**, *53*, 151–158. [CrossRef]
14. Ma, X.; Westmana, E.; Slakera, B.; Thibodeaub, D.; Counter, D. The b-value evolution of mining-induced seismicity and mainshock occurrences at hard-rock mines. *Int. J. Rock Mech. Min. Sci.* **2018**, *104*, 64–70. [CrossRef]
15. Zhao, Y.; Yang, T.H.; Liu, H.L.; Wang, S.H.; Zhang, P.H.; Jia, P.; Wang, X.R. A path for evaluating the mechanical response of rock masses based on deep mining-induced microseismic data: A case study. *Tunn. Undergr. Space Technol.* **2021**, *15*, 104025. [CrossRef]
16. Islam, M.R.; Shinjo, R. Mining-induced fault reactivation associated with the main conveyor belt roadway and safety of the Barapukuria Coal Mine in Bangladesh: Constraints from BEM simulations. *Int. J. Coal Geol.* **2009**, *79*, 115–130. [CrossRef]
17. Potvin, Y.; Troncoso, J.J.; Wesseloo, J. Interpretation of seismic data and numerical modelling of fault reactivation at El Teniente, Reservas Norte sector. *Min. Technol.* **2010**, *119*, 175–181. [CrossRef]
18. Li, X.B.; Weng, L. Numerical investigation on fracturing behaviors of deep-buried opening under dynamic disturbance. *Tunn. Undergr. Space Technol.* **2016**, *54*, 61–72. [CrossRef]
19. Meng, N.K.; Bai, J.B.; Chen, Y.; Wang, X.Y.; Wu, W.D.; Wu, B.W. Stability analysis of roadside backfill body at gob-side entry retaining under combined static and dynamic loading. *Eng. Fail. Anal.* **2021**, *127*, 105531. [CrossRef]
20. Zhu, W.C.; Li, Z.H.; Zhu, L.; Tang, C.A. Numerical simulation on rockburst of underground opening triggered by dynamic disturbance. *Tunn. Undergr. Space Technol.* **2010**, *25*, 587–599. [CrossRef]